ACT001 suppresses ox-LDL-mediated macrophage ferroptosis via activating the NRF2 pathway: An *in vitro* mechanistic study relevant to atherosclerosis

YANGYANG TAO[1*], YUWU CHEN[2*], YONGHOU ZHAO[1] and JIANBO CAI[1]

[1]Department of Neurology, Heilongjiang Mental Hospital, Harbin, Heilongjiang 150000, P.R. China; [2]Department of Cardiology, The Second Affiliated Hospital, Harbin Medical University, State Key Laboratory of Frigid Zone Cardiovascular Diseases, Harbin, Heilongjiang 150000, P.R. China

Received May 5, 2026; Accepted August 19, 2026

DOI: 10.3892/etm.2026.13287

Abstract. Oxidized low-density lipoprotein (ox-LDL) is a key inducer of ferroptosis, which is associated with the progression of atherosclerosis. Macrophages play a notable role in atherosclerosis development, and ferroptosis in these cells contributes to the pathological process of atherosclerosis. However, the potential intervention strategy for ox-LDL-induced RAW264.7 cell ferroptosis remains unclear. ACT001 has emerged as a novel anti-inflammation agent; therefore, *in vitro* experiments were conducted to elucidate the specific effects and mechanism of ACT001 on ox-LDL-induced ferroptosis in RAW264.7 cells. RAW264.7 cells were treated with ox-LDL to establish an *in vitro* ferroptosis model and then co-treated with ACT001. Consequently, the expression of ferroptosis-related markers were evaluated via western blotting, PCR/detection of lipid peroxidation markers (malondialdehyde, glutathione; SOD: Superoxide dismutase; 4-HNE: 4-Hydroxynonenal; lipid reactive oxygen species (ROS) content)/transmission electron microscopy/iron content assay/mitochondrial membrane potential assay and ferrous ion staining. The potential molecular mechanism of ACT001 was further explored by detecting the expression and nuclear translocation of nuclear factor E2-related factor 2 (NRF2) via western blotting, confocal immunofluorescence/CHIP-PCR. Ox-LDL significantly mediated ferroptosis in RAW264.7 cells, as evidenced by increased lipid peroxidation, decreased glutathione content, elevated ROS production and downregulated expression of glutathione peroxidase 4 (GPX4) and solute carrier family 7 member 11 (xCT); however, co-treatment with ACT001 effectively reversed these changes. Mechanistically, ACT001 treatment significantly increased the nuclear translocation of NRF2 and enhanced the enrichment of NRF2 level in the promoter regions of GPX4 and xCT via binding with NRF2, thereby upregulating the expression of GPX4 and xCT. In conclusion, ACT001 effectively ameliorated ox-LDL-triggered ferroptosis in RAW264.7 macrophages through facilitating NRF2 nuclear translocation and upregulating GPX4/xCT expression. The present *in vitro* findings revealed a molecular mechanism linking ACT001 to the inhibition of macrophage ferroptosis, offering preliminary cell-level evidence of the ACT001 therapeutic potential against macrophage-driven pathological events in atherosclerosis.

Introduction

Epidemiological research has indicated an annual increase in the incidence of ischemic cardiovascular diseases. Atherosclerosis is the primary pathological basis of various ischemic conditions, including stroke and coronary heart disease (1-4). Contemporary research on therapeutic strategies for atherosclerosis predominantly emphasizes lipid-lowering and anti-inflammatory approaches; however, these strategies have not yet substantially reduced the incidence and mortality rates linked to atherosclerosis (5,6). Consequently, there is a need to explore innovative therapeutic approaches for the treatment of atherosclerosis.

Atherosclerosis is characterized as a chronic inflammatory disease impacting the vascular wall, with macrophages serving as key immune cells integral to the initial and advanced phases of the disease (7). During the early phase, endothelial cells dysfunction facilitates the adhesion of circulating monocytes to the arterial wall, where they differentiate into macrophages and engage in lipid phagocytosis (8). Macrophages that ingest lipids are predisposed to differentiate into M1-type pro-inflammatory macrophages, thereby intensifying the local inflammatory response within atherosclerotic plaques (9,10). In the advanced stage of atherosclerosis, the phagocytic capacity of macrophages declines, and a marked number

Correspondence to: Professor Jianbo Cai or Professor Yonghou Zhao, Department of Neurology, Heilongjiang Mental Hospital, 5 Guoyuan Street, Harbin, Heilongjiang 150000, P.R. China
E-mail: jianbocai123123@163.com
E-mail: zyh101180@163.com

*Contributed equally

Key words: ACT001, glutathione peroxidase 4, solute carrier family 7 member 11, atherosclerosis

of macrophages undergo apoptosis, further exacerbating the inflammatory response and increasing plaque instability (11,12). As a result, targeting the inflammatory response and apoptosis of macrophages is regarded as a promising strategy for ameliorating atherosclerosis.

Ferroptosis represents a relatively recently identified form of programmed cell death, characterized by membrane lipid peroxidation and oxidative stress. Previous studies have established the involvement of macrophage ferroptosis in the progression of atherosclerosis (13-15). Notable proteins in the ferroptotic pathway include glutathione peroxidase 4 (GPX4) and solute carrier family 7 member 11 (SLC7A11, also known as xCT), which catalyze lipid peroxides and facilitate glutathione (GSH) transport (16,17). A diminution in the expression levels of xCT and GPX4 results in a redox imbalance and lipid peroxidation of cell membranes. In advanced atherosclerotic plaques, a pronounced decrease in the expression of GPX4 and xCT within macrophages has been documented, whereas overexpression of GPX4 ameliorates atherosclerosis progression (18-20). Consequently, targeting ferroptosis in macrophages may be a promising therapeutic strategy for attenuating atherosclerosis. Nuclear factor erythroid 2-related factor 2 (NRF2) is a prototypical transcription factor, which regulates the activity and expression of GPX4, xCT and superoxide dismutase (SOD), thereby mitigating ferroptosis (21,22).

ACT001 is a chemically optimized derivative of micheliolide, a natural sesquiterpene lactone derived from parthenolide (23,24). Parthenolide has been documented to modulate oxidative stress and ferroptosis across various cell types (25), and exerts protective effects on cardiomyocytes against doxorubicin-induced ferroptosis by activating NRF2 signaling (26,27). Similarly, micheliolide has recently been shown to mitigate atherosclerosis by inhibiting macrophage ferroptosis through the disruption of the Kelch-like ECH-associated protein 1 (KEAP1)-NRF2 interaction (12). This provides a chemical and pharmacological basis for the hypothesis that ACT001 may exert comparable protective effects in oxidized low-density lipoprotein (ox-LDL)-stimulated macrophages. While existing research on ACT001 has primarily focused on its NF-κB inhibitory anti-inflammatory function (28-33), there is growing evidence of its intrinsic antioxidant capacity, characterized by reactive oxygen species (ROS) scavenging and NRF2 pathway activation in microglia, alveolar macrophages and cardiomyocytes. Mechanistically, ox-LDL induces macrophage ferroptosis primarily through the inactivation of NRF2, depletion of GSH, downregulation of GPX4 and xCT, excessive lipid peroxidation and accumulation of labile iron (34,35). Given that NRF2 serves as the central transcription factor mitigating the ferroptotic cascade, we hypothesized that ACT001 could mitigate ox-LDL-induced macrophage ferroptosis by enhancing NRF2-mediated antioxidant signaling, in addition to its well-documented anti-inflammatory activity through NF-κB suppression. Moreover, ACT001 exhibits superior translational potential compared with natural parthenolide, as evidenced by its progression to Phase II clinical trials for glioblastoma treatment with confirmed biosafety (36,37). Despite these indicative findings, to the best of our knowledge, no prior research has elucidated whether ACT001 modulates ox-LDL-induced macrophage ferroptosis within AS. Consequently, the present *in vitro* study was designed to elucidate the NRF2-dependent molecular mechanisms underlying the anti-ferroptotic effects of ACT001 in macrophages in the context of atherosclerosis.

Materials and methods

Drugs (ACT001). ACT001 was purchased from MedChemExpress (HY-128861B, purity: ≥98%, 250 mg). Meanwhile, according to the results of Cell Counting Kit (CCK)-8, the cell viability was significantly reduced at the concentration of 20 μM (Fig. S1). Consequently, 10 μM was selected as the treatment concentration for the *in vitro* experiment.

Cell culture. RAW264.7 (Procell; cat. no. CL-0190) were pretreated with 5 μM ML385 (MedChemExpress, HY-100523) for 1 h at 37˚C. RAW264.7 cells were cultured in RAW 264.7 cell specific medium (Procell; cat. no. CM-0190). In addition, RAW264.7 were treated with 100 μg/ml ox-LDL (MedChemExpress, HY-NP013) for 48 h at 37˚C (12). Cells were passaged at 80-90% confluence to maintain a stable phenotype. Culture medium was removed, and cells were rinsed with sterile PBS to remove residual serum. Cells were detached using prewarmed (37˚C) trypsin-EDTA, monitored microscopically and neutralized with complete serum-containing medium. The cell suspension was centrifuged, the supernatant was discarded and the pellet was resuspended in fresh medium. Cells were routinely subcultured at a 1:2 ratio, adjusted according to experimental needs. The initial seeding density was 5,000-10,000 cells per cm^2.

Experimental design. A model of ox-LDL-induced ferroptosis was developed in RAW264.7 macrophages to initially assess the protective effects of 10 μM ACT001 (≥98% purity) against ferroptosis. This was achieved by evaluating several ferroptosis markers, including lipid peroxidation, GSH levels, iron content, mitochondrial damage and the expression of GPX4/xCT. Subsequently, cytoplasmic/nuclear fractionation, immunofluorescence and chromatin immunoprecipitation (ChIP)-PCR assays were employed to verify that ACT001 promotes the nuclear translocation of NRF2 and enhances its binding to the promoters of GPX4 and xCT. The NRF2-specific inhibitor ML385 was further utilized in rescue experiments to confirm the role of NRF2 in the anti-ferroptotic effects mediated by ACT001. This comprehensive analysis elucidates the molecular mechanism by which ACT001 inhibits ferroptosis in macrophages.

CCK-8 assay. After treating RAW264.7 (0.00, 1.25, 2.50, 5.00 μM/10.00 μM/20.00 μM ACT001, 24 h, 37˚C), 10 μl CCK-8 working solution (C0037; Beyotime Biotechnology) was added to Dulbecco's Modified Eagle Medium and incubated in 96-well plates for 1 h (37˚C). The absorbance was then measured at 460 nm.

Reverse transcription-quantitative PCR (RT-qPCR). Total RNA was extracted from treated RAW264.7 cells using TRIzol reagent (Invitrogen; Thermo Fisher Scientific, Inc.). In brief, cells were subjected to chloroform phase separation,

Table I. Primer sequences of GPX4, xCT and GAPDH.

Gene name	Forward	Reverse
GPX4	TGTGCATCCCGCGATGATT	CCCTGTACTTATCCAGGCAGA
xCT	GGCACCGTCATCGGATCAG	CTCCACAGGCAGACCAGAAAA
NRF2	CTTTAGTCAGCGACAGAAGGAC	AGGCATCTTGTTTGGGAATGTG
HO-1	AGGTACACATCCAAGCCGAGA	CATCACCAGCTTAAAGCCTTCT
GAPDH	TGGCCTTCCGTGTTCCTAC	GAGTTGCTGTTGAAGTCGCA

GPX, glutathione peroxidase; xCT, solute carrier family 7 member 11; HO, heme oxygenase.

followed by isopropanol precipitation, serial ethanol washes and reconstitution in DEPC-treated water. The RNA concentration was determined through UV spectrophotometry and any genomic DNA contamination was eliminated via DNase I digestion prior to cDNA synthesis. First-strand cDNA synthesis was performed using 0.5 μg of total RNA with a Roche reverse transcription kit (Roche Diagnostics), adhering to the manufacturer's thermal cycling protocol. RT-qPCR was carried out using the Roche SYBR Green master mix (Roche Diagnostics) in a 10 μl reaction system to quantify *GPX4* and *xCT* mRNA levels. Thermocycling conditions were as follows: Initial 10-min denaturation step at 95˚C, followed by 40 cycles of 95˚C for 15 sec (denaturation), 60˚C for 60 sec (annealing and extension), and concluded with melting curve analysis for validation. Relative mRNA expression levels were calculated using the $2^{-\Delta\Delta Cq}$ method (38), employing GAPDH as the internal reference. Primer sequences are provided in Table I.

Western blot analysis. Total protein was extracted from RAW264.7 cells using RIPA buffer (P0013B, Beyotime Biotechnology), supplemented with 1 mM phenylmethylsulfonyl fluoride (PMSF) (MedChemExpress, HY-B0496). Protein concentrations were determined utilizing the BCA kit (P0009; Beyotime Biotechnology), and samples were standardized to a concentration of 3 μg/μl. Proteins were separated on a 10% SDS-PAGE gel (20 μg protein/per lane), initially at 80 V for 30 min, followed by 120 V for 100 min, and subsequently transferred onto PVDF membranes (MilliporeSigma). Membranes were blocked with 5% non-fat milk for 1 h at room temperature and then incubated overnight at 4˚C with primary antibodies from CST Biological Reagents Co., Ltd. (all 1:1,000: GPX4 (#52455), xCT (#98051), GAPDH (#2118), Histone H3 (#4499) and NRF2 (#12721). Following washes with TBS-T (0.1% Tween), the blots were incubated with HRP-conjugated secondary antibody (1:10,000; A0208; Beyotime Biotechnology) for 1 h at 25˚C, rinsed and visualized using an enhanced chemiluminescent kit (PE0010; Beijing Solarbio Science & Technology Co., Ltd.) on a Tanon imaging system (Tanon Science and Technology Co., Ltd.). Band intensities were semi-quantified with ImageJ version 1.4 (National Institutes of Health), using GAPDH as the loading control. The data are presented as representative blots and quantitative bar graphs.

Nuclear protein/cytoplasmic protein extraction. The nuclear/cytoplasmic proteins were extracted by Biyuntian nuclear and cytoplasmic isolation kit (P0028; Beyotime Biotechnology). Specifically, the cells were rinsed with PBS, scraped off with a cell scraper, collected by centrifugation. The cell supernatant was removed and the cell precipitation was left for later use. A total of 200 μl of PMSF supplemented cytoplasmic protein extraction reagent A was added to 20 μl of cell precipitation. Following this, the sample was vortexed at maximum speed for 5 sec, until the cell precipitate was completely suspended and dispersed. The cell mixture was then incubated in an ice bath for 10-15 min. Then 10 μl of cytosolic protein extraction reagent B was added, and the samples was vortexed at maximum speed for 5 sec, then was placed in an ice bath for 1 min. After incubation, the sample was vortexed again at maximum speed for 5 sec and then centrifuged at 4˚C, 12,000-16,000 x g for 5 min. The supernatant, which contained the extracted cytoplasmic protein, was immediately transferred into a precooled plastic tube. For precipitation, the remaining supernatant was completely aspirated and 50 μl of nuclear protein extraction reagent supplemented with PMSF was added. The sample was vortexed at maximum speed for 15-30 sec, until the cell precipitate was completely suspended and dispersed. The sample was then put back into the ice bath and was subjected to high-speed vigorous vortexing for 15-30 sec every 1-2 min for a total of 30 min. The sample was centrifuged at 12,000-16,000 x g for 10 min at 4˚C. After centrifugation, the supernatant, which contained the extracted nuclear protein, was immediately transferred into a pre-cooled plastic tube. For nuclear proteins, Histone H3 was used as loading control protein. For cytoplasmic proteins, GAPDH was used as loading control protein.

Malondialdehyde (MDA) level and SOD activity. MDA content and SOD activity in RAW264.7 were determined using commercial assay kits (S0131 and S0101M, respectively; Beyotime Biotechnology). Absorbance values were measured at 532 and 450 nm, respectively, following the manufacturer's instructions. Data are presented as bar graphs.

GSH levels. Intracellular GSH levels in RAW264.7 were measured using a GSH assay kit (A006-2-1; Nanjing Jiancheng Bioengineering Institute) according to the provided protocol. After treatment, cells were treated with 100 μl ice-cold PBS and 100 μl precipitating solution. The mixture was centrifuged at 1,348 x g for 10 min, and the supernatant was incubated with 125 μl working solution for 5 min. Absorbance at 405 nm was detected using an LMax Microplate Reader (Molecular

Devices, LLC), and GSH concentrations were normalized to total protein content. Results are shown as bar graphs.

Measurement of 4-HNE. Measurement of 4-HNE levels was performed using the 4-HNE assay kit (cat. no. ab238538, Abcam). In total, 50 μl standards or samples were added to each well of the 4-HNE conjugate-coated plate, followed by a 10-min incubation. Fifty microliters of diluted anti-4-HNE antibody was then added to each well, and the plate was incubated for 1 h. Each well was washed with 250 μl 1X Wash Buffer. One hundred microliters of diluted secondary antibody-HRP conjugate was added to every well, and samples were incubated for another 1 h before repeating the washing procedure using 1x Wash Buffer. Next, 100 μl of substrate solution was dispensed into each well, and incubation was carried out for 2-20 min. The enzymatic reaction was terminated by adding 100 μl of stop solution to each well. Absorbance values were immediately measured with a microplate reader at a wavelength of 450 nm.

Iron content assay. Iron concentrations in macrophages were quantified using an Iron Assay Kit (Leagene; cat. no. TC1016, Beijing Regen Biotechnology Co., Ltd.). Following the manufacturer's protocol, absorbance was measured in blank wells, iron standard solutions and experimental samples. Iron levels were calculated via colorimetric analysis and displayed as bar graphs.

Transmission electron microscopy. Mitochondrial ultrastructure was observed using transmission electron microscopy. Macrophages were centrifuged (25˚C) at 1,000 x g for 20 min and the supernatant was removed. Cells were pre-fixed with 2.5% glutaraldehyde overnight at 4˚C, followed by post-fixation with 1% osmium tetroxide in cacodylate buffer for 1 h at 25˚C, dehydrated in a graded ethanol series and embedded in Poly/Bed 812 resin at 60˚C for 24 h. Ultrathin sections (70 nm) were prepared and stained with uranyl acetate for 15 min and lead citrate for 10 min at 25˚C. Mitochondrial morphology was compared among groups. Representative images and quantitative bar graphs are shown.

Lipid peroxidation determination (lipid ROS levels). Lipid peroxidation in RAW264.7 was detected by flow cytometry. After treatment, cells were washed with PBS (BL302A; Biosharp Life Sciences) and digested with trypsin-EDTA (C0201; Beyotime Biotechnology). Harvested cells were stained with 10 μM C11-BODIPY 581/591 lipid peroxidation sensor (S0043M; Beyotime Biotechnology, excitation: 581 nm, emission: 591 nm) in serum-free medium at 37˚C for 30 min in the dark. Cells were resuspended in ice-cold PBS, filtered through a 40 μm mesh, and analyzed by flow cytometry (Attune NxT, Thermo Fisher). Data were processed with FlowJo v10.8.1, (BD Biosciences). Data are presented as flow cytometric histograms and bar graphs.

Mitochondrial membrane potential assay and ferrous ion staining. RAW264.7 were seeded in 48-well plates and treated according to experimental groups. Mitochondrial membrane potential was measured using a detection kit (C2006; Beyotime Biotechnology), and ferrous ions were stained with FerroOrange (F374; Dojindo Laboratories, Inc.), after staining, live-cell fluorescence images were captured using an inverted fluorescence microscope. The mean fluorescence intensity of each channel was quantified from five randomly selected fields of view/well using ImageJ (version 1.8.0.345) software (National Institutes of Health) and normalized to the number of DAPI-stained nuclei. All staining procedures were performed following the manufacturer's protocols. Results are shown as fluorescence images and quantitative bar graphs.

Total ROS/mitochondrial ROS. Total intracellular and mitochondrial ROS levels were measured using Dichlorodihydrofluorescein diacetate (Beyotime Biotechnology) and MitoSOX Red mitochondrial superoxide indicator (Thermo Fisher Scientific, Inc.), respectively. After treatment, RAW 264.7 were washed twice with ice-cold PBS and incubated with DCFH-DA or MitoSOX at room temperature for 30 min in the dark. After two additional washes, fluorescence intensity was observed under a fluorescence microscope and quantitatively analyzed with Image-Pro Plus (version 11.1) (39). The mean fluorescence intensity of each group was normalized to the control group and the results were presented as fold-change relative to the control.

Immunofluorescence. Samples were fixed in cold acetone for 10 min at 25˚C and washed three times with PBS. Cells were blocked with 5% bovine serum albumin (Beijing Solarbio Science & Technology Co., Ltd.) containing 0.3% Triton X-100 at room temperature for 1 h. The primary antibody against NRF2 (1:300; #12721; Cell Signaling Technology, Inc.) was applied and incubated overnight at 4˚C. After washing, fluorescently labeled goat anti-rabbit secondary antibody (1:500; ab150077; Abcam) was added and incubated for 2 h at room temperature. Nuclei were counterstained with DAPI for 5 min at 25˚C. Images were captured using a fluorescence microscope (LSM 800, Zeiss).

ChIP-PCR. The binding of NRF2 to the promoters of HO-1, GPX4 and xCT was analyzed using the Pierce™ Agarose ChIP Kit (Thermo Fisher Scientific, Inc.; cat. no 26156). Protein-DNA complexes were cross-linked with 4% paraformaldehyde for 15 min at 25˚C and fragmented by sonication. Immunoprecipitation was performed using anti-NRF2 antibody (1:100; #12721; Cell Signaling Technology, Inc.) or rabbit IgG (1:100; #66362; Cell Signaling Technology, Inc.). 30 μl of agarose beads were added overnight at 4˚C with gentle rotation. The bead-antigen-antibody complexes were sequentially washed with low-salt wash buffer, once with high-salt wash buffer, once with LiCl wash buffer and twice with TE buffer to remove non-specifically bound proteins and DNA. Cross-links were reversed by heating at 65˚C for 4 h in the presence of proteinase K to digest bound proteins, and DNA was purified. Enrichment of target promoter regions was quantified by RT-qPCR. Results are presented as bar graphs.

Statistical analysis. All experimental data are presented as the mean ± standard error of the mean, and each dataset was derived from at least three independent experimental replicates. For statistical comparisons, data conforming to a normal distribution were analyzed using an unpaired

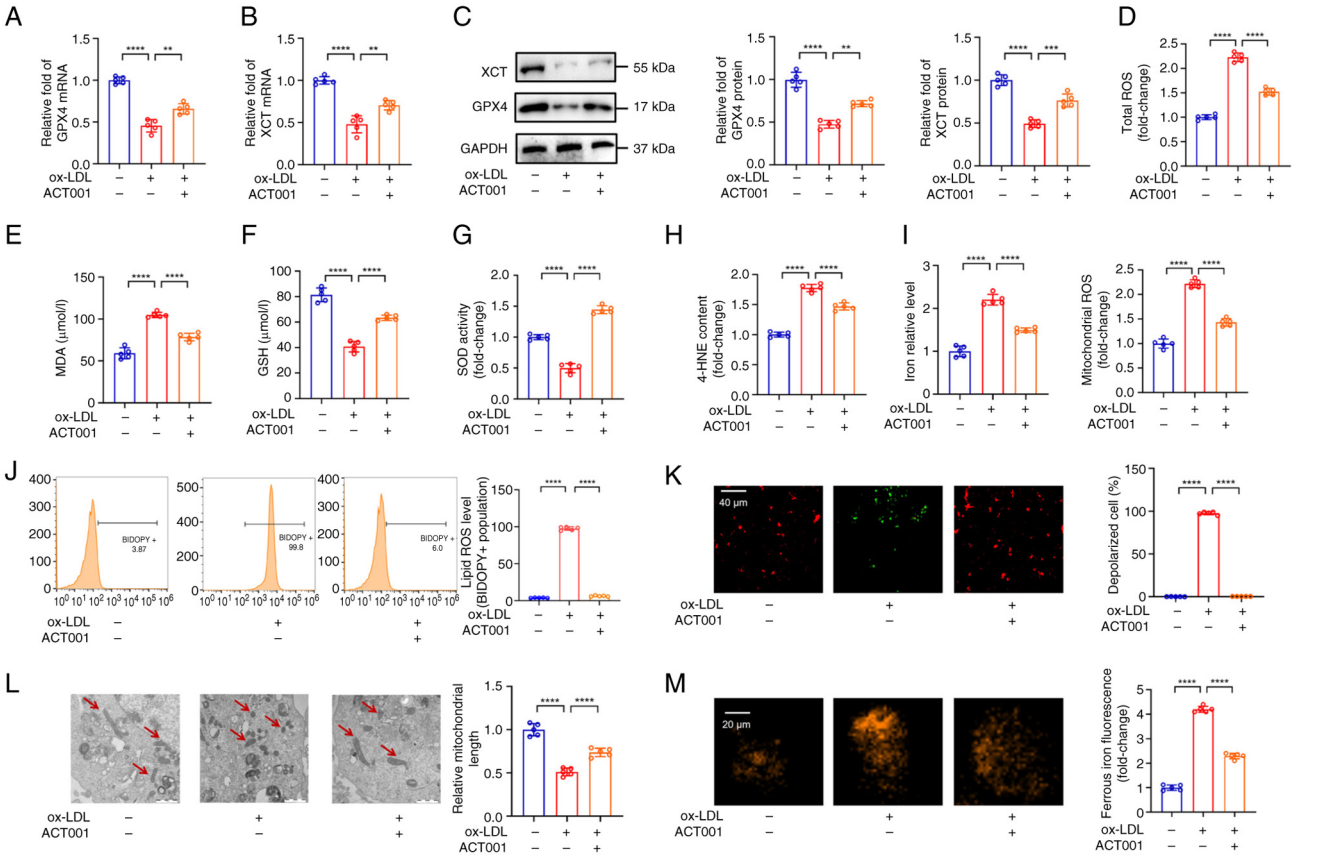

Figure 1. ACT001 inhibits RAW 264.7 cell ferroptosis *in vitro*. (A) The *GPX4* mRNA level of RAW 264.7 cells under ox-LDL administration with or without ACT001 pre-treatment, (n=5). (B) The *xCT* mRNA level of RAW 264.7 under ox-LDL administration with or without ACT001 pre-treatment, (n=5). (C) The GPX4 and xCT protein level of RAW 264.7 under ox-LDL administration with or without ACT001 pre-treatment, (n=5). (D) The total ROS and mitochondrial ROS level of RAW 264.7 under ox-LDL administration with or without ACT001 pre-treatment, (n=5). (E) The MDA content of RAW 264.7 under ox-LDL administration with or without ACT001 pre-treatment, (n=5). (F) The GSH content of RAW 264.7 under ox-LDL administration with or without ACT001 pre-treatment, (n=5). (G) The SOD activity of RAW 264.7 under ox-LDL administration with or without Fer-1 pre-treatment, (n=5). (H) The 4-HNE content of RAW 264.7 under ox-LDL administration with or without ACT001 pre-treatment, (n=5). (I) The iron relative level of RAW 264.7 under ox-LDL administration with or without ACT001 pre-treatment, (n=5). (J) Lipid ROS level was evaluated by flow cytometry using C11-Bodipy fluorescent probe, (n=5). (K) Representative images for mitochondrial membrane potential, (n=5). (L) Representative transmission electron microscopy images of RAW 264.7 and the quantification of relative mitochondrial length, (n=5). Arrow, mitochondria. (M) Representative ferrous iron concentration images and quantification of RAW 264.7 in different treatment groups by confocal immunofluorescence assay (n=5). Results are expressed as mean ± SD. Comparisons of parameters were performed with one-way ANOVA with Bonferroni post hoc test. **P<0.01; ***P<0.001; ****P<0.0001. GPX4, glutathione peroxidase 4; xCT, solute carrier family 7 member 11; ROS, reactive oxygen species; ox-LDL, oxidized low density lipoprotein; SOD, superoxide dismutase; MDA, malondialdehyde; GSH, glutathione; 4-HNE, 4-hydroxynonenal.

two-tailed Student's t-test when comparing two groups. For multiple group comparisons, one-way analysis of variance was performed, followed by the Bonferroni post hoc test to assess pairwise differences. All statistical analyses were carried out using SPSS software (version 21.0; IBM Corp.). P<0.05 was considered to indicate a statistically significant difference.

Results

ACT001 inhibits RAW 264.7 ferroptosis mediated by ox-LDL. First, the cytotoxicity of ACT001 on RAW264.7 cells was evaluated *in vitro* (treated for 24 h) and the cell viability was significantly reduced at the concentration of 20 μM (Fig. S1). Consequently, 10 μM was selected as the treatment concentration for the *in vitro* experiment. Subsequently, ox-LDL was used to induce ferroptosis in RAW264.7 cells and ACT001 to pretreat RAW264.7 cells *in vitro*. RT-qPCR and western blot analyses revealed a significant reduction in the expression levels of GPX4/xCT in ox-LDL group, which was improved after ACT001 administration (Fig. 1A-C). Meanwhile, the up-regulation of total and mitochondrial ROS levels in RAW264.7 cells induced by ox-LDL was ameliorated by ACT001 (Fig. 1D). Furthermore, lipid peroxidation, a hallmark of ferroptosis, was evaluated by measuring the levels of MDA and 4-Hydroxynonenal (4-HNE), which serve as biomarkers of this process. *In vitro* assays indicated a significant increase in MDA and 4-HNE concentrations in the ox-LDL-treated group, which were notably ameliorated by ACT001 treatment. Additionally, ox-LDL treatment resulted in decreased SOD and GSH levels, which were also improved by ACT001 administration (Fig. 1E-H).

Additionally, ACT001 effectively reduced the elevated concentration of iron ions in RAW264.7 induced by ox-LDL (Fig. 1I). Furthermore, the present findings indicated that ox-LDL increased lipid ROS levels, a condition that could be ameliorated by ACT001 (Fig. 1J). In addition, the mitochondrial membrane potential was assessed using JC-1 staining, revealing that ACT001 significantly mitigated the loss of

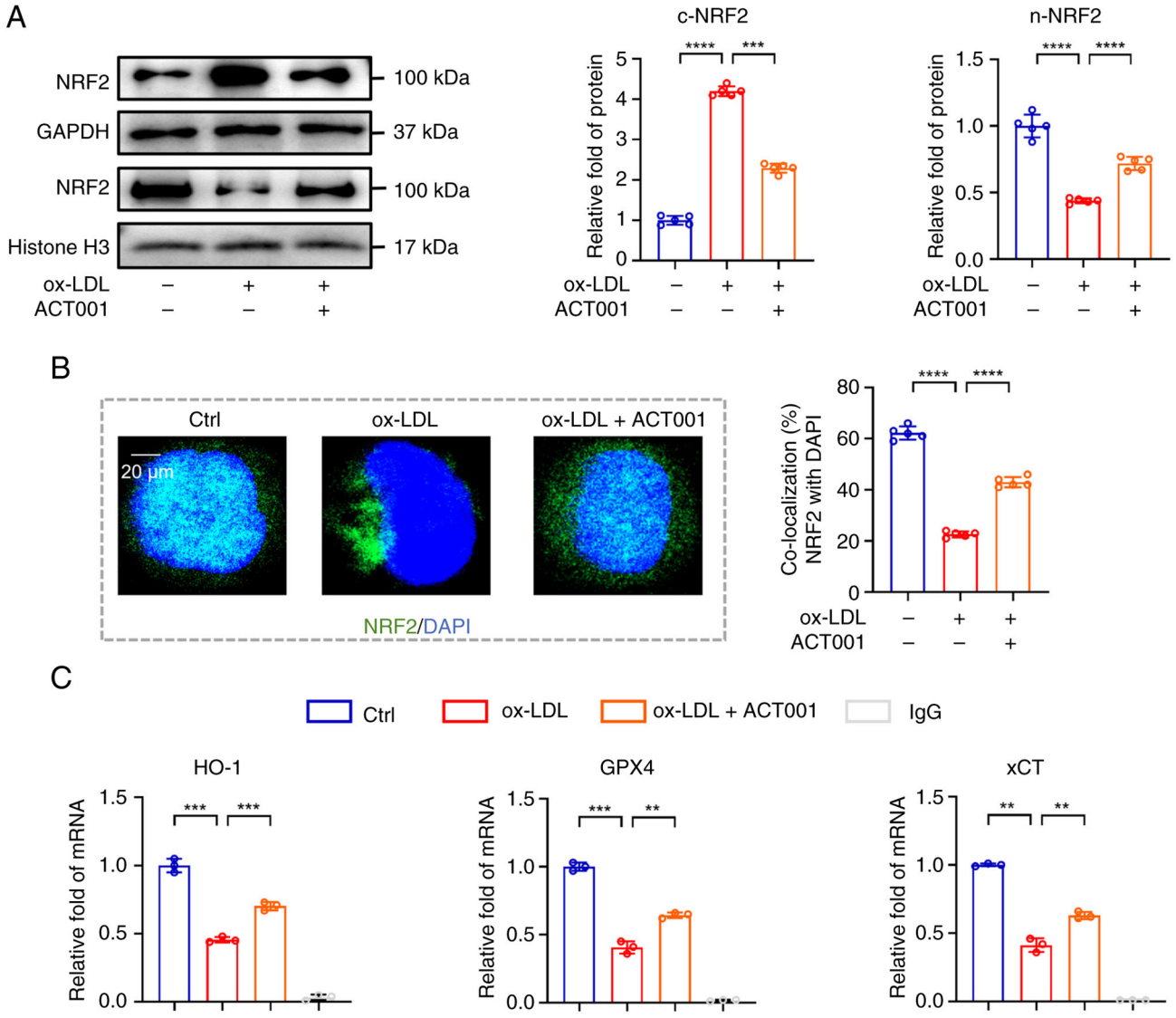

Figure 2. ACT001 promotes NRF2 nuclear translocation *in vitro*. (A) NRF2 protein level of RAW 264.7 under ox-LDL administration, (n=5). (B) Confocal fluorescent staining is used to evaluate the nuclear translocation of NRF2. (C) The enrichment ability of NRF2 on HO-1, GPX4 and xCT promoter using Chromatin immunoprecipitation-PCR; (n=5). Results are expressed as mean ± SD. Comparisons of parameters were performed with one-way ANOVA with Bonferroni post hoc test. **P<0.01; ***P<0.001; ****P<0.0001. GPX4, glutathione peroxidase 4; xCT, solute carrier family 7 member 11; HO-1, heme oxygenase-1; NRF2, Nuclear factor erythroid 2-related factor 2; c-, cytoplasmic; n-nuclear.

membrane potential caused by ox-LDL (Fig. 1K). Transmission electron microscopy was used to examine the mitochondrial morphology of RAW264.7 cells. The results indicated that RAW264.7 cultured with ox-LDL exhibited mitochondrial damage and characterized by reduced mitochondrial size and swollen or absent mitochondrial cristae. By contrast, pretreatment with ACT001 significantly prevented these ultrastructural mitochondrial alterations in RAW264.7 (Fig. 1L). Additionally, ACT001 administration could reduce the ferrous iron concentrations in RAW264.7 treated with ox-LDL (Fig. 1M). Hence, these findings suggested that ACT001 could inhibit RAW264.7 ferroptosis mediated by ox-LDL.

ACT001 administration inhibited RAW 264.7 ferroptosis via mediating NRF2 nuclear translocation. It was hypothesized that ACT001 might mediate the NRF2 nuclear translocation, thereby increasing the expression of GPX4 and xCT in RAW264.7. To investigate this, cytoplasmic and nuclear lysates were extracted from RAW264.7 subjected to different treatment conditions. The findings indicated that ox-LDL down-regulated NRF2 protein expression in nuclear lysates while significantly increasing its levels in cytoplasmic lysates (Fig. 2A); these observations were corroborated by immunofluorescence analyses (Fig. 2B). Furthermore, ChIP-PCR experiments revealed that NRF2 bound to the promoter sequences of GPX4 and xCT. Compared with the ox-LDL group, ACT001 administration significantly increased the enrichment of NRF2 levels at the heme oxygenase-1 (HO-1), GPX4 and xCT promoter sequences (Fig. 2C).

ACT001 treatment inhibited RAW264.7 ferroptosis via promoting the activation of NRF2 pathway. ML385, a specific NRF2 inhibitor, was used to pretreat the RAW264.7 cells. The findings indicated that the upregulation in GPX4 and xCT mRNA/protein expression in the ox-LDL + ACT001 group was significantly reversed by ML385 (Fig. 3A-C).

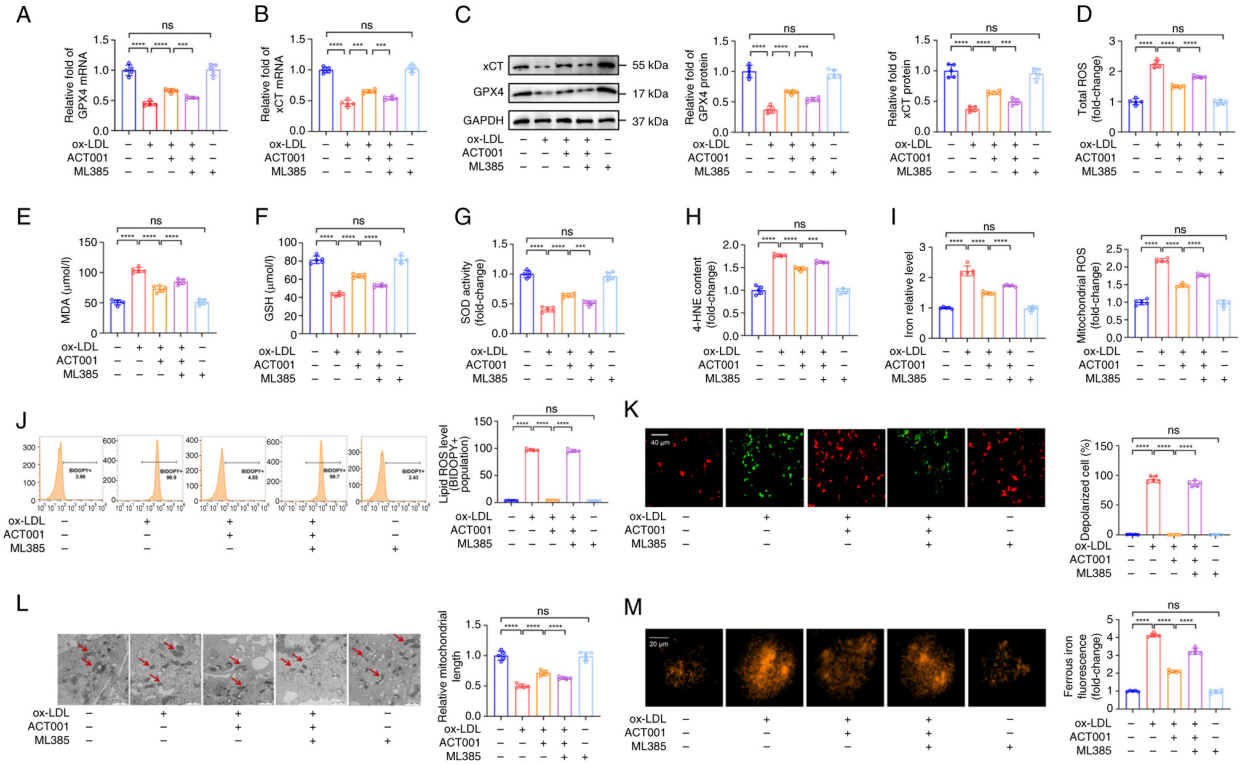

Figure 3. ACT001 treatment inhibits RAW 264.7 ferroptosis via promoting the activation of NRF2 pathway. (A) The *GPX4* mRNA level of RAW264.7 under ox-LDL administration with or without ML385 pre-treatment, (n=5). (B) The *xCT* mRNA level of RAW264.7 under ox-LDL administration with or without ML385 pre-treatment, (n=5). (C) The GPX4 and xCT protein level of RAW264.7 under ox-LDL administration with or without ML385 pre-treatment, (n=5). (D) The total ROS and mitochondrial ROS level of RAW264.7 under ox-LDL administration with or without ML385 pre-treatment, (n=5). (E) The MDA content of RAW264.7 under ox-LDL administration with or without ML385 pre-treatment, (n=5). (F) The GSH content of RAW264.7 under ox-LDL administration with or without ML385 pre-treatment, (n=5). (G) The SOD activity of RAW264.7 under ox-LDL administration with or without ML385 pre-treatment, (n=5). (H) The 4-HNE content of RAW264.7 under ox-LDL administration with or without ML385 pre-treatment, (n=5). (I) The iron relative level of RAW264.7 under ox-LDL administration with or without ML385 pre-treatment, (n=5). (J) The lipid ROS level was evaluated by flow cytometry using C11-Bodipy fluorescent probe, (n=5). (K) Representative images for mitochondrial membrane potential, (n=5). (L) Representative transmission electron microscopy images of RAW264.7 and the quantification of relative mitochondrial length, (n=5). (M) Representative ferrous iron concentration images and quantification of RAW264.7 in different treatment groups by confocal immunofluorescence assay (n=5). Results are expressed as mean ± SD. Comparisons of parameters were performed with one-way ANOVA with Bonferroni post hoc test. ***P<0.001; ****P<0.0001. GPX4, glutathione peroxidase 4; xCT, solute carrier family 7 member 11; ROS, reactive oxygen species; ox-LDL, oxidized low density lipoprotein; SOD, superoxide dismutase; MDA, malondialdehyde; GSH, glutathione; 4-HNE, 4-hydroxynonenal.

Furthermore, compared with the ox-LDL + ACT001 group, a marked increase in both total and mitochondrial ROS was observed in the ox-LDL + ACT001 + ML385 group (Fig. 3D). Additionally, in comparison with the ox-LDL + ACT001 group, the levels of iron content, 4-HNE and MDA were also increased in the ox-LDL + ACT001 + ML385 treated group. Alternatively, ML385 decreased GSH levels and SOD activity in the ox-LDL + ACT001 + ML385 group (Fig. 3E-I). C11-BODIPY staining revealed that ML385 also increased the lipid ROS levels in the ox-LDL + ACT001 + ML385 group (Fig. 3J). Transmission electron microscopy and JC-1 staining revealed that ML385 aggravated mitochondrial damage (Fig. 3K and L). Meanwhile, ML385 treatment increased the concentration of ferrous iron in RAW264.7 treated with ox-LDL + ACT001 (Fig. 3M). These data indicated that ACT001 treatment inhibited RAW 264.7 ferroptosis via promoting the activation of the NRF2 pathway.

Discussion

Macrophage ferroptosis contributes to the advancement of atherosclerosis by intensifying the inflammatory response and enlarging the necrotic core (40,41). Therefore, targeting ferroptosis in macrophages may represent a transformative therapeutic strategy. ACT001 has shown considerable efficacy in alleviating inflammatory diseases (23,24). Nevertheless, the role and underlying mechanisms of ACT001 in macrophage ferroptosis triggered by ox-LDL remain inadequately elucidated. In the present *in vitro* cellular experiments, two principal findings were identified: i) ACT001 inhibited ox-LDL-mediated macrophage ferroptosis by up-regulating GPX4 and xCT; and ii) the protective effect relied on NRF2 pathway activation. These cellular observations provide mechanistic insights into the pathological events that drive atherosclerosis.

NRF2 possesses a zinc finger domain that facilitates its binding to DNA sequences, thereby enabling its function as a transcription factor (42,43). NRF2 regulates the transcription of proteins involved in anti-inflammatory and antioxidant responses, positioning it as a potential therapeutic target for various chronic diseases (44,45). In the context of atherosclerosis, several compounds have been identified to enhance oxidative stress homeostasis by activating NRF2, thereby inhibiting the progression of atherosclerosis. For example,

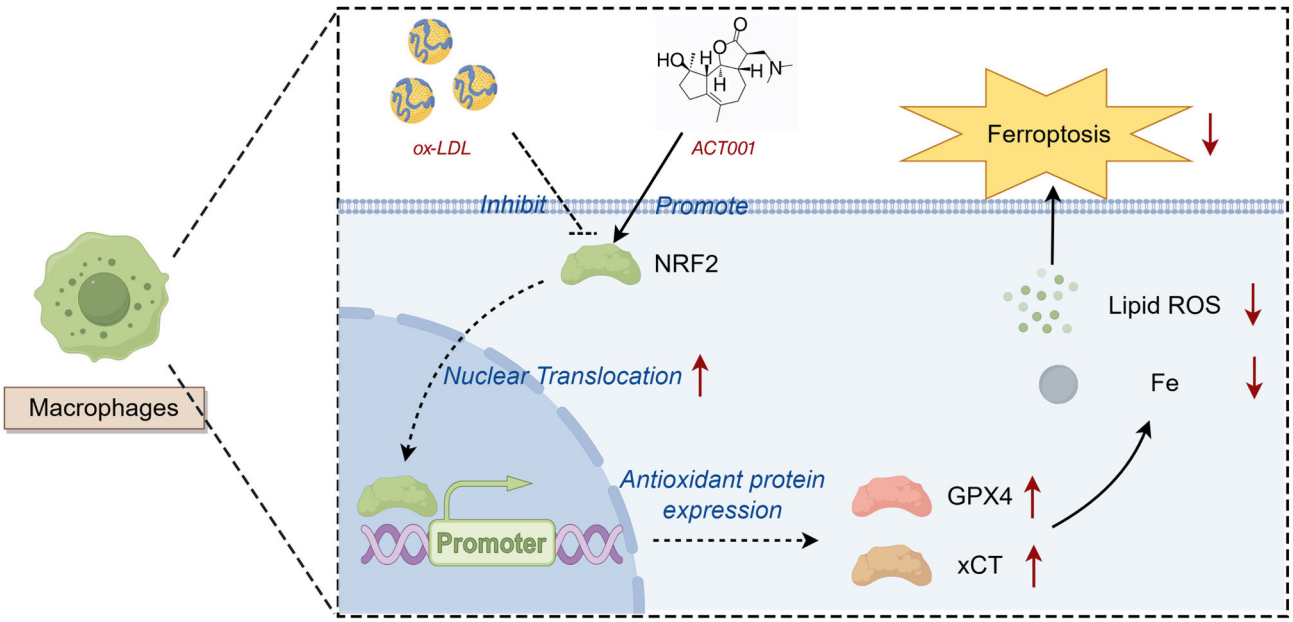

Figure 4. Molecular mechanism of ox-LDL-induced macrophage ferroptosis inhibited by ACT001.

quercetin, a flavonoid, has been demonstrated to attenuate atherosclerosis development through activation of the NRF2 pathway (46). In the present study, ACT001 was identified as a novel small-molecule NRF2 agonist, and the findings indicated that ACT001 increases nuclear NRF2 levels and enhances the expression of GPX4/xCT in macrophages treated with ox-LDL. Furthermore, ACT001 ameliorated lipid peroxidation and reduced oxidative stress; however, the NRF2-specific inhibitor ML385 negated the protective effects of ACT001 on ferroptosis, demonstrating that ACT001 effectively inhibits macrophage ferroptosis, which demonstrate that ACT001 exerts anti-ferroptotic activity on macrophages, a critical cell type participating in atherosclerotic lesion formation.

Previous research has established that KEAP1 modulates the activity of NRF2 through direct binding. This interaction inhibits NRF2 stability, facilitating its ubiquitination and degradation. Conversely, disruption of the KEAP1/NRF2 interaction enhances NRF2 nuclear translocation and activation (47-49). Direct binding to NRF2 can also augment its activity (42,50).

The anti-tumor efficacy of ACT001 in the treatment of lung cancer and glioma is well-documented (37,51-53). The present *in vitro* cellular data demonstrated that ACT001 relieved ox-LDL-induced macrophage ferroptosis, a pathological process linked to cardiovascular atherosclerotic injury. This observation suggests at potential cardiovascular protective properties of ACT001 beyond its known anti-tumor activity, although further *in vivo* atherosclerosis models are required for validation. Furthermore, existing studies have suggested that ACT001 may attenuate neurological and joint inflammation (24,54). Future research should focus on elucidating the potential role of ACT001 in the management of chronic inflammatory diseases.

The present study has several limitations. First, there is a lack of subsequent investigations at the animal level concerning the protective effects of ACT001 against atherosclerosis and macrophage ferroptosis. Second, the concentration-dependent mechanisms by which ACT001 modulates ferroptosis have not been comprehensively examined. Third, the present study utilized a singular concentration of 10 μM ACT001 for all *in vitro* functional and mechanistic validations, without constructing a comprehensive dose-response curve. CCK-8 cytotoxicity assay confirmed that a concentration of 20 μM ACT001 resulted in significant cell death in RAW264.7 cells, whereas 10 μM was identified as a safe, non-toxic concentration that provided substantial protective effects against ox-LDL-induced ferroptosis. The primary aim of the present study was to elucidate the downstream molecular pathways connecting ACT001 to NRF2 activation and the subsequent up-regulation of GPX4/xCT, rather than to systematically explore the full pharmacological dose-response profile of ACT001. Future *in vivo* atherosclerosis experiments should incorporate multi-gradient concentration treatments and quantitative pharmacodynamic curve analyses to characterize the dose-dependent efficacy of ACT001.

In conclusion, ACT001 interacts with NRF2 to facilitate NRF2 nuclear translocation, upregulate GPX4 and xCT expression and suppress ox-LDL-triggered macrophage ferroptosis. This cell-level mechanism provides preliminary mechanistic evidence for targeting macrophage ferroptosis as a means to interfere with the pathological processes driving atherosclerosis; further *in vivo* studies are necessary to verify its efficacy against systemic atherosclerotic lesions (Fig. 4).

Acknowledgements

Not applicable.

Funding

The present study was supported by the Natural Science Foundation of Heilongjiang Province (grant no. JJ2025BS0050),

Fund of Key Laboratory of Myocardial Ischemia, Ministry of Education (grant nos. KF202514, KF202308, KF202313, and KF202410).

Availability of data and materials

The data generated in the present study may be requested from the corresponding author.

Authors' contributions

YT and YC performed the experiments, analyzed the data and wrote the manuscript. YZ and JC designed the study. YT, YC, YZ and JC confirm the authenticity of all the raw data. All the authors have read and approved the final version of manuscript.

Ethics approval and consent to participate

Not applicable.

Patient consent for publication

Not applicable.

Competing interests

The authors declare that they have no competing interests.

References

1. Kong P, Cui ZY, Huang XF, Zhang DD, Guo RJ and Han M: Inflammation and atherosclerosis: Signaling pathways and therapeutic intervention. Signal Transduct Target Ther 7: 131, 2022.
2. Libby P: The changing landscape of atherosclerosis. Nature 592: 524-533, 2021.
3. Tan T, Cui H, Zhu E and Lai Y: Calcific aortic valve disease and atherosclerotic cardiovascular disease: Shared and distinct mechanisms and treatment strategies. Cardiac Research 2: 12-20, 2026.
4. Cai J: Cardiac Research: A new journal in cardiovascular medicine-leading the way in cardiovascular innovation. Cardiac Res 1: 1-2, 2025.
5. Wolf D and Ley K: Immunity and inflammation in atherosclerosis. Circ Res 124: 315-327, 2019.
6. Kobiyama K and Ley K: Atherosclerosis. Circ Res 123: 1118-1120, 2018.
7. Martinez-Campanario MC, Cortés M, Han L, Brischetto A, Rivero-Soriano P, Font-Díaz J, Maurel J, Andrés V and Postigo A: Lipid-laden macrophages in atherosclerosis and cancer. Semin Cancer Biol 117: 38-56, 2025.
8. Wang B, Tang X, Yao L, Wang Y, Chen Z, Li M, Wu N, Wu D, Dai X, Jiang H and Ai D: Disruption of USP9X in macrophages promotes foam cell formation and atherosclerosis. J Clin Invest 132: e154217, 2022.
9. Barrett TJ: Macrophages in atherosclerosis regression. Arterioscler Thromb Vasc Biol 40: 20-33, 2020.
10. Kuznetsova T, Prange KHM, Glass CK and de Winther MPJ: Transcriptional and epigenetic regulation of macrophages in atherosclerosis. Nat Rev Cardiol 17: 216-228, 2020.
11. Tabas I and Bornfeldt KE: Macrophage phenotype and function in different stages of atherosclerosis. Circ Res 118: 653-667, 2016.
12. Luo X, Wang Y, Zhu X, Chen Y, Xu B, Bai X, Weng X, Xu J, Tao Y, Yang D, *et al*: MCL attenuates atherosclerosis by suppressing macrophage ferroptosis via targeting KEAP1/NRF2 interaction. Redox Biol 69: 102987, 2024.
13. Jiang M, Xu X and Zhu G: Ferroptosis of macrophages and endothelial cells in atherosclerosis: Molecular mechanisms and therapeutic targets. Rev Cardiovasc Med 26: 45117, 2025.
14. Wu X, Li J, Cheng H and Wang L: Ferroptosis and lipid metabolism in acute myocardial infarction. Rev Cardiovasc Med 25: 149, 2024.
15. Elkammash A, Zaki A, Tawfik O and Gouda S: Ferroptosis: A key driver in atherosclerosis progression and arterial disease. Rev Cardiovasc Med 25: 441, 2024.
16. Mou Y, Wang J, Wu J, He D, Zhang C, Duan C and Li B: Ferroptosis, a new form of cell death: Opportunities and challenges in cancer. J Hematol Oncol 12: 34, 2019.
17. Bell HN, Stockwell BR and Zou W: Ironing out the role of ferroptosis in immunity. Immunity 57: 941-956, 2024.
18. Bao X, Luo X, Bai X, Lv Y, Weng X, Zhang S, Leng Y, Huang J, Dai X, Wang Y, *et al*: Cigarette tar mediates macrophage ferroptosis in atherosclerosis through the hepcidin/FPN/SLC7A11 signaling pathway. Free Radic Biol Med 201: 76-88, 2023.
19. Lin Q, Ding S, Shi M, Cao Y, Liu J, Sun D, Xu W, Pang S, Gu A and Mingyan E: Tricetin attenuates atherosclerosis by suppressing macrophage ferroptosis via activation of the NRF2 pathway. Int Immunopharmacol 143: 113418, 2024.
20. De Meyer GRY, Zurek M, Puylaert P and Martinet W: Programmed death of macrophages in atherosclerosis: Mechanisms and therapeutic targets. Nat Rev Cardiol 21: 312-325, 2024.
21. Liu J, Pang SY, Zhou SY, He QY, Zhao RY, Qu Y, Yang Y and Guo ZN: Lipocalin-2 aggravates blood-brain barrier dysfunction after intravenous thrombolysis by promoting endothelial cell ferroptosis via regulating the HMGB1/Nrf2/HO-1 pathway. Redox Biol 76: 103342, 2024.
22. Wei R, Zhao Y, Wang J, Yang X, Li S, Wang Y, Yang X, Fei J, Hao X, Zhao Y, *et al*: Tagitinin C induces ferroptosis through PERK-Nrf2-HO-1 signaling pathway in colorectal cancer cells. Int J Biol Sci 17: 2703-2717, 2021.
23. Tong L, Li J, Li Q, Wang X, Medikonda R, Zhao T, Li T, Ma H, Yi L, Liu P, *et al*: ACT001 reduces the expression of PD-L1 by inhibiting the phosphorylation of STAT3 in glioblastoma. Theranostics 10: 5943-5956, 2020.
24. Cai L, Gong Q, Qi L, Xu T, Suo Q, Li X, Wang W, Jing Y, Yang D, Xu Z, *et al*: ACT001 attenuates microglia-mediated neuroinflammation after traumatic brain injury via inhibiting AKT/NFκB/NLRP3 pathway. Cell Commun Signal 20: 56, 2022.
25. LoBianco FV, Krager KJ, Johnson E, Godwin CO, Allen AR, Crooks PA, Compadre CM, Borrelli MJ and Aykin-Burns N: Parthenolide induces rapid thiol oxidation that leads to ferroptosis in hepatocellular carcinoma cells. Front Toxicol 4: 936149, 2022.
26. Carlisi D, De Blasio A, Drago-Ferrante R, Di Fiore R, Buttitta G, Morreale M, Scerri C, Vento R and Tesoriere G: Parthenolide prevents resistance of MDA-MB231 cells to doxorubicin and mitoxantrone: The role of Nrf2. Cell Death Discov 3: 17078, 2017.
27. Sun J, Qian L, Guo F, Gai F and Lin P: Parthenolide mitigates doxorubicin-induced cardiotoxicity in rats with associated activation of Nrf2 and inhibition of ferroptosis. J Biochem Mol Toxicol 39: e70626, 2025.
28. Luo H, Liu X, Liu H, Wang Y, Xu K, Li J, Liu M, Guo J and Qin X: ACT001 Ameliorates ionizing radiation-induced lung injury by inhibiting NLRP3 inflammasome pathway. Biomed Pharmacother 163: 114808, 2023.
29. Fu Q, Shen N, Fang T, Zhang H, Di Y, Liu X, Du C and Guo J: ACT001 alleviates inflammation and pyroptosis through the PPAR-γ/NF-κB signaling pathway in LPS-induced alveolar macrophages. Genes Genomics 46: 323-332, 2024.
30. Lei X, Li S, Luo C, Wang Y, Liu Y, Xu Z, Huang Q, Zou F, Chen Y, Peng F and Long H: Micheliolide attenuates lipopolysaccharide-induced inflammation by modulating the mROS/NF-κB/NLRP3 axis in renal tubular epithelial cells. Mediators Inflamm 2020: 3934769, 2020.
31. Zhong J, Gong W, Chen J, Qing Y, Wu S, Li H, Huang C, Chen Y, Wang Y, Xu Z, *et al*: Micheliolide alleviates hepatic steatosis in db/db mice by inhibiting inflammation and promoting autophagy via PPAR-γ-mediated NF-κB and AMPK/mTOR signaling. Int Immunopharmacol 59: 197-208, 2018.
32. Xu Z, Xu J, Sun S, Lin W, Li Y, Lu Q, Li F, Yang Z, Lu Y and Liu W: Mecheliolide elicits ROS-mediated ERS driven immunogenic cell death in hepatocellular carcinoma. Redox Biol 54: 102351, 2022.
33. Kalantary-Charvadeh A, Sanajou D, Hemmati-Dinarvand M, Marandi Y, Khojastehfard M, Hajipour H, Mesgari-Abbasi M, Roshangar L and Nazari Soltan Ahmad S: Micheliolide protects against doxorubicin-induced cardiotoxicity in mice by regulating PI3K/Akt/NF-kB signaling pathway. Cardiovasc Toxicol 19: 297-305, 2019.
34. Zhu X, Chen Y, Xu B, Mou J, Wang M, Gu Q, Sun Q, Li M, Zhao C, Zeng M, *et al*: Targeting KEAP1/NRF2 interaction with oleuropein ameliorates atherosclerosis by inhibiting macrophage ferroptosis. Free Radic Biol Med 240: 566-582, 2025.

35. Srivastava N, Hu H, Peterson OJ, Vomund AN, Stremska M, Zaman M, Giri S, Li T, Lichti CF, Zakharov PN, *et al*: CXCL16-dependent scavenging of oxidized lipids by islet macrophages promotes differentiation of pathogenic $CD8^+$ T cells in diabetic autoimmunity. Immunity 57: 1629-1647.e8, 2024.
36. Yang J, Li Y, Han X, Pei X, Lin Z and Li C: The antitumor effect of the novel agent MCL/ACT001 in pancreatic ductal adenocarcinoma. J Cancer Res Clin Oncol 149: 5717-5728, 2023.
37. Xi X, Liu N, Wang Q, Chu Y, Yin Z, Ding Y and Lu Y: ACT001, a novel PAI-1 inhibitor, exerts synergistic effects in combination with cisplatin by inhibiting PI3K/AKT pathway in glioma. Cell Death Dis 10: 757, 2019.
38. Livak KJ and Schmittgen TD: Analysis of relative gene expression data using real-time quantitative PCR and the 2(-Delta Delta C(T)) method. Methods 25: 402-408, 2001.
39. Hu Y, Yu J, Cui X, Zhang Z, Li Q, Guo W, Zhao C, Chen X, Meng M, Li Y, *et al*: Combination usage of adipocount and image-pro plus/ImageJ software for quantification of adipocyte sizes. Front Endocrinol (Lausanne) 12: 642000, 2021.
40. Xue S, Su Z and Liu D: Immunometabolism and immune response regulate macrophage function in atherosclerosis. Ageing Res Rev 90: 101993, 2023.
41. Cao L, Zhang J, Yu L, Yang W, Qi W, Ren R, Liu Y, Hou Y, Cao Y, Li Q, *et al*: E3 ubiquitin ligase Listerin regulates macrophage cholesterol efflux and atherosclerosis by targeting ABCA1. J Clin Invest 135: e186509, 2025.
42. Zhang DD: Thirty years of NRF2: Advances and therapeutic challenges. Nat Rev Drug Discov 24: 421-444, 2025.
43. Yamamoto M, Kensler TW and Motohashi H: The KEAP1-NRF2 system: A thiol-based sensor-effector apparatus for maintaining redox homeostasis. Physiol Rev 98: 1169-1203, 2018.
44. Patıroğlu T, Murataldı S, Özkul Y and Köklü E: Report of a family with fanconi anemia and ataxia-telangiectasia. Turk J Haematol 21: 33-37, 2004.
45. Dong Y, Zheng M, Ding W, Guan H, Xiao J and Li F: Nrf2 activators for the treatment of rare iron overload diseases: From bench to bedside. Redox Biol 81: 103551, 2025.
46. Luo X, Weng X, Bao X, Bai X, Lv Y, Zhang S, Chen Y, Zhao C, Zeng M, Huang J, *et al*: A novel anti-atherosclerotic mechanism of quercetin: Competitive binding to KEAP1 via Arg483 to inhibit macrophage pyroptosis. Redox Biol 57: 102511, 2022.
47. Bollong MJ, Lee G, Coukos JS, Yun H, Zambaldo C, Chang JW, Chin EN, Ahmad I, Chatterjee AK, Lairson LL, *et al*: A metabolite-derived protein modification integrates glycolysis with KEAP1-NRF2 signalling. Nature 562: 600-604, 2018.
48. Dhyani N, Tian C, Gao L, Rudebush TL and Zucker IH: Nrf2-Keap1 in cardiovascular disease: Which is the cart and which the horse? Physiology (Bethesda) 39: 0, 2024.
49. Ge W, Zhao K, Wang X, Li H, Yu M, He M, Xue X, Zhu Y, Zhang C, Cheng Y, *et al*: iASPP Is an antioxidative factor and drives cancer growth and drug resistance by competing with Nrf2 for Keap1 binding. Cancer Cell 32: 561-573.e6, 2017.
50. Muzammil K, Sabah Ghnim Z, Saeed Gataa I, Fawzi Al-Hussainy A, Ali Soud N, Adil M, Ali Shallan M and Yasamineh S: NRF2-mediated regulation of lipid pathways in viral infection. Mol Aspects Med 97: 101279, 2024.
51. Zhao M, Qin T and Huang D: ACT001 inhibits the proliferation of non-small cell lung cancer cells by upregulating NKTR expression. Thorac Cancer 13: 1772-1782, 2022.
52. Ding XJ, Mei T, Xi XN, Wang JY, Wang WJ, Chen Y, Lu YX, Qin TT and Huang DZ: ACT001 suppresses the malignant progression of small-cell lung cancer by inhibiting lactate production and promoting anti-tumor immunity. Thorac Cancer 16: e70028, 2025.
53. Li Q, Sun Y, Liu B, Li J, Hao X, Ge W, Zhang X, Bao S, Gong J, Jiang Z, *et al*: ACT001 modulates the NF-κB/MnSOD/ROS axis by targeting IKKβ to inhibit glioblastoma cell growth. J Mol Med (Berl) 98: 263-277, 2020.
54. Li Y, Yang JY, Lin ML, Liu TZ, Lu WN, Yang Y, Liu ZC, Li JH, Zhang GQ and Guo JS: ACT001 improves OVX-induced osteoporosis by suppressing the NF-κB/NLRP3 signaling pathway. Mol Med 31: 131, 2025.